TORCH physics performance: improving low-momentum PID performance during Upgrade IB and beyond

T. Hadavizadeh[1], S. Bhasin[2], T. Blake[3], M. Flavia Cicala[3], R. Forty[4], C. Frei[4],
E. P. M. Gabriel[5], S. Gambetta[5], R. Gao[1], T. Gershon[3], T. Gys[4], , T. H. Hancock[1],
N. Harnew[1], M. Kreps[3], E. J. Millard[3], F. Muheim[5], D. Piedigrossi[4], J. Rademacker[2],
M. Van Dijk[4], G. Wilkinson[1].

[1]*University of Oxford, United Kingdom*
[2]*University of Bristol, United Kingdom*
[3]*University of Warwick, United Kingdom*
[4]*CERN, Switzerland*
[5]*University of Edinburgh, United Kingdom*

Abstract

This document details the status of simulation studies for the proposed TORCH detector for operation during Upgrade Ib. The anticipated physics performance in key processes is presented, alongside a summary of the R&D status. Further studies of interest are outlined.

Contents

1 Introduction

This document discusses the TORCH detector and the physics benefits introduced by augmenting the particle identification capabilities of LHCb with time-of-flight during Upgrade Ib. The TORCH (Time Of internally Reflected CHerenkov light) detector measures the time-of-flight (ToF) of charged particles over large areas, providing positive particle identification (PID) of pions, kaons and protons up to $10\,\mathrm{GeV}/c$ momentum and beyond [1]. The difference in ToF between pions and kaons over a $\sim$10 m flight path at $10\,\mathrm{GeV}/c$ is 35 ps, hence TORCH aims for a time resolution of $\sim$10-15 ps per track for a 3σ separation.

The PID capability of the current LHCb detector is provided by the RICH system [2]. This has proved essential in the discrimination of pions, kaons and protons for most of its physics measurements, for example in CP-violation, exotic spectroscopy and particle tagging. However, the RICH system provides no positive kaon or proton identification below $\sim$10 GeV/c. Therefore the proposal is to install TORCH immediately upstream of RICH2, located $\sim$9.5 m from the proton-proton interaction region [3,4]. The experimental arrangement is then shown in Fig. 1. At this location, the total area of TORCH would be $5 \times 6\,\mathrm{m}^2$, divided into 18 modules, each 66 cm wide and 2.5 m high. The installation of TORCH is well suited for the start-up of LHC Run 4, with installation into LHCb in the Long Shutdown 3 (LS3) during 2024/5.

TORCH combines timing measurements with DIRC-style reconstruction, a technique pioneered by the BaBar DIRC [5] and Belle II TOP [6,7] collaborations. TORCH exploits the prompt production of Cherenkov light in planes of 1 cm thick quartz to time the arrival of the charged particles, which also facilitates a modular design. Cherenkov photons travel to the periphery of the quartz plates by total internal reflection where they are reflected by a cylindrical mirror surface of a quartz block. The block focuses the photons onto
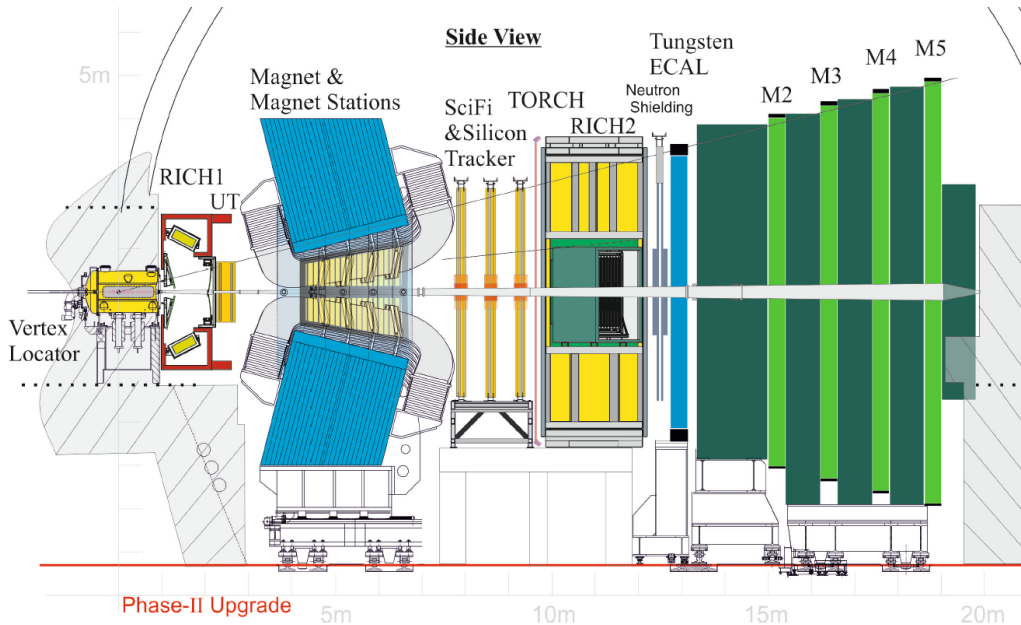

Figure 1: A schematic of the LHCb experiment, showing TORCH located directly upstream of the RICH2 detector.
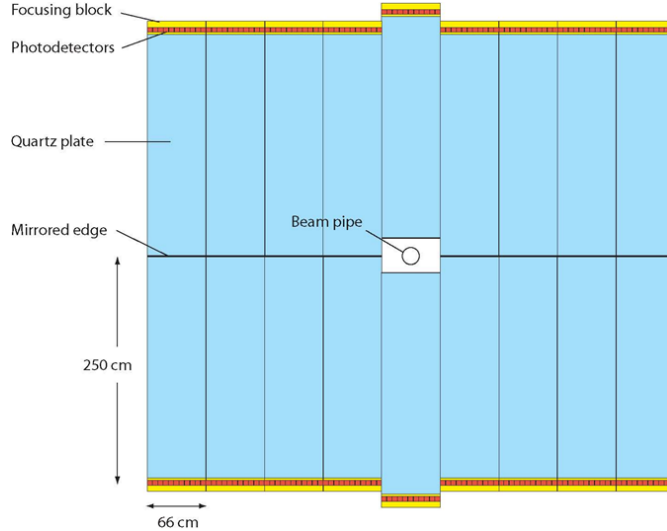
Figure 2: The TORCH modular arrangement.

a plane of pixellated Micro-Channel Plate Photomultipliers (MCP-PMTs) where their positions and arrival times are measured. The expectation is that typically 30 photons will be detected per charged track, hence the required ToF resolution dictates the timing of single photons to a precision of around 70 ps.

Schematic arrangements of the TORCH geometry in the longitudinal and transverse planes are shown in Figs. 2 and 3, showing the modular arrangement and focussing block. Each module is instrumented with 11 MCP-PMTs. For every photon hit in the MCP-PMTs, the Cherenkov angle θ_c and the photon path length of propagation through the quartz L is measured. From knowledge of the dispersion relation within the quartz, a correction for chromatic dispersion is then made to the photon time of propagation. From simulation, a ~ 1 mrad precision is required on the measurement of the angles in both planes to achieve the required intrinsic timing resolution [1].

In order to achieve the above precision, TORCH requires MCP-PMTs with a fine granularity in the focussing direction and a coarse granularity in the non-focussing direction. The pixel structure of the MCP-PMTs has been customized to meet TORCH requirements, each having an anode granularity of 128×8 effective pixels, with a $53 \times 53 \, \text{mm}^2$ active area on a 60 mm pitch. This effective pixelisation in the fine-granularity direction is achieved by exploiting charge sharing between 64 physical anodes. A major focus of the TORCH project thus far has been the development of the MCP-PMTs, which has been conducted in collaboration with an industrial partner, Photek Ltd. (UK).[1] A series of MCP-PMTs has been prototyped by Photek and has been used in the measurements presented below [8]. A customized electronics system [9] adopting the NINO32 and HPTDC chipsets has also been employed.

Studies have evaluated the performance of TORCH in the LHCb experiment using a full GEANT4 simulation. A luminosity of $2 \times 10^{33} \, \text{cm}^{-2} \, \text{s}^{-1}$ appropriate for Run 4 has been simulated, including collision pile-up, and is presented in this document. The track entry point in the quartz radiator of TORCH is needed for photon reconstruction, and has been provided by fully reconstructed real tracks from the upgraded tracking system.

---

[1]Photek Ltd., 26 Castleham Road, St Leonards on Sea, East Sussex, TN38 9NS, United Kingdom.
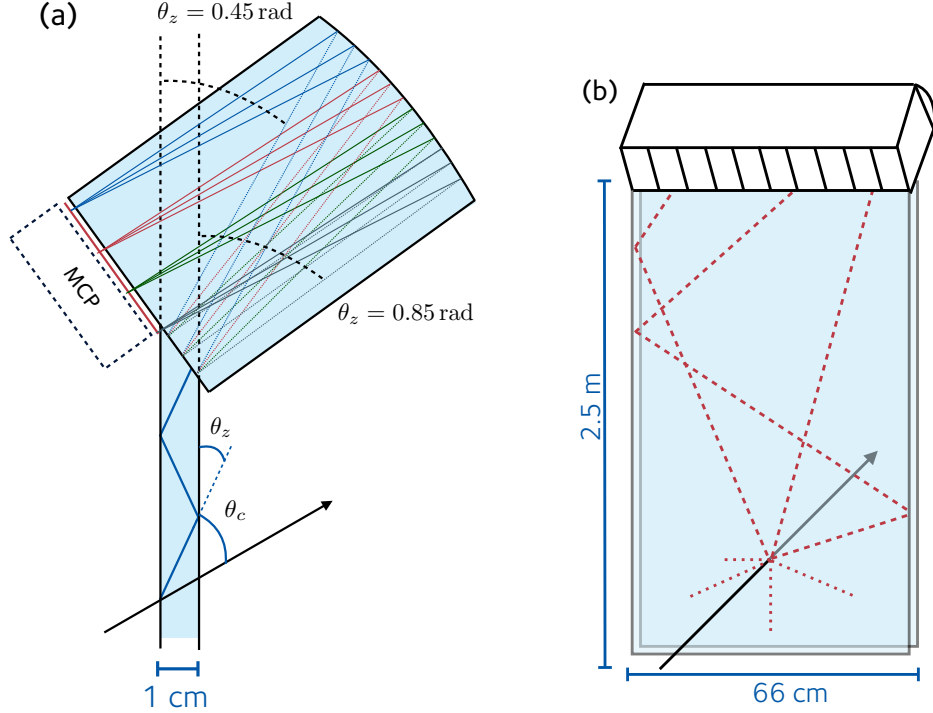
Figure 3: Schematics of a TORCH module showing possible reflection paths: (a) the focussing block and MCP-PMT plane, (b) a single LHCb TORCH module.

The TORCH reconstruction algorithm computes the expected hit distributions for the $\pi/K/p$ hypotheses and compares them to the MCP-PMT photon spatial hits and arrival times, and log-likelihoods are then computed.

Studies of the performance of TORCH at a luminosity of $1 \times 10^{34}\,\mathrm{cm}^{-2}\,\mathrm{s}^{-1}$ for Upgrade II have started. Initial results indicate that whilst there is some drop in performance with respect to Upgrade Ib due to higher occupancy, the expectation is that the kaon and proton efficiencies can be maintained with an increase of photon-detector granularity in the central regions. Whilst too early to present in this document, work is ongoing to optimize these results as a function of detector parameters (granularity, focussing, backgrounds *etc.*).

This document is arranged as follows. Section 2 outlines the results of measurements taken from prototype TORCH modules in $5\,\mathrm{GeV}/c$ mixed pion-proton beams at the CERN PS. Section 3 details GEANT4 simulation studies of TORCH incorporated into the LHCb experiment. Section 4 reports simulations of some key physics channels and tagging performance, before and after the introduction of the TORCH detector. Finally, Section 5 discusses future work.

2 Status of latest beam tests

2.1 Summary of beam tests

Three beam test campaigns have been carried out at the East Hall T9 facility at CERN. The first two, undertaken in November 2017 and June 2018, used a small-scale TORCH
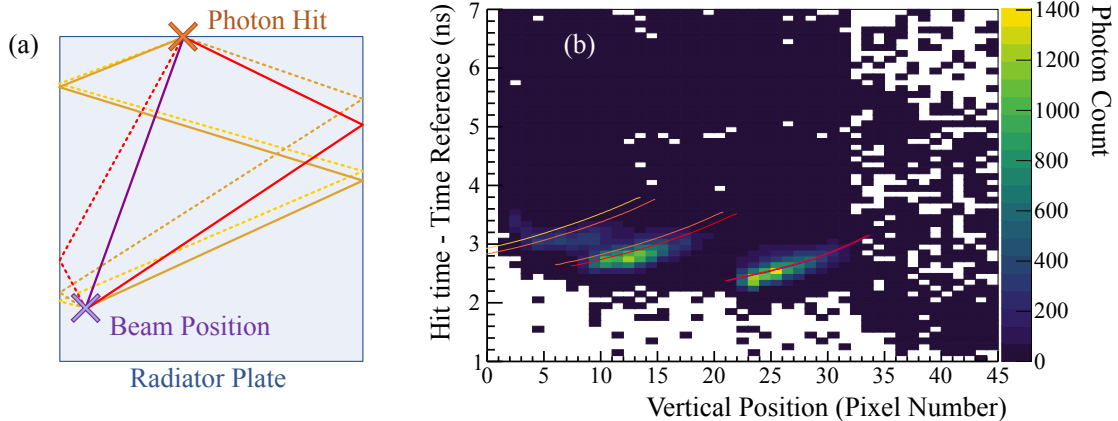
Figure 4: (a) Orders of reflection within the radiator plate. Direct photons and those reflecting first off the right hand edge are solid lines, while those reflecting first off the left hand edge are dotted. Colour corresponds to the number of edge reflections: direct is purple, one reflection is red, two orange, and three yellow. (b) Photon count as a function of arrival time and vertical detector position for data taken during the June 2018 beam test. The overlaid lines show the predicted time of arrival, with colours matching (a). For red and orange, where there are two lines of the same colour, the one beginning at the smaller time is dotted in (a). As the reflections fall on the lower half of the detector, the upper 20 pixels have been excluded from the plot range.

module, named from here on "Mini-TORCH", with dimensions $120 \times 350 \times 10\,\mathrm{mm}^3$. The final beam test, carried out in October 2018, used a half-height TORCH module, named "Proto-TORCH", with dimensions $660 \times 1250 \times 10\,\mathrm{mm}^3$. Analysis of data taken in the first two beam tests is nearing completion, with measurements of the single photon timing resolution of Mini-TORCH made, while analysis of data taken in the final beam test is still ongoing.

In each beam test a pair of borosilicate fingers, each instrumented by a single channel MCP, is used to provide a time reference signal. Two pressurised CO_2 Cherenkov detectors are used to provide external discrimination between protons and pions in the beam.

2.2   Single photon timing resolution

The single photon timing resolution is measured through comparison of the detected time of arrival of photons to that predicted in offline calculations. For this to be possible, the different paths photons take through the radiator plate, referred to as the order of reflection and shown in Fig. 4a, must be separated in the data. This is achieved by comparing the vertical position (*i.e.* the position of fine-granularity in the MCP-PMT) at which a photon is detected with the time it arrived, an example of which is shown in Fig. 4b. Three distinct peaks can be seen, corresponding to different orders of reflection from the side of the radiator bar. Through directing the beam at the edge of the radiator plate, pairs of orders can be made to coincide in time, allowing them to be treated together and simplifying the separation.

Comparing the detected photon arrival time to the predictions shown by the coloured lines overlaid onto Fig. 4b gives a residual distribution such as the one shown in Fig. 5. The width of this distribution, $\sigma_{measured}$, can be used to determine the single photon
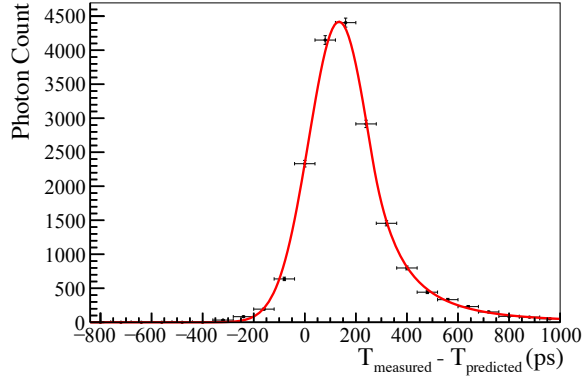
4

Figure 5: The residual distribution of the time of direct photons from Fig. 4 to the predicted time of arrival. A crystal ball fit is used to model the shape. The tail of the distribution is attributed to the electronics used to read out the MCP detector.

resolution of Mini-TORCH

$$\sigma^2_{TORCH} = \sigma^2_{measured} - \sigma^2_{beam} - \sigma^2_{timeref}, \tag{1}$$

where σ_{beam} is a spread in the photon arrival time due to beam spread, and $\sigma_{timeref}$ is the resolution of the time reference against which TORCH timestamps are measured. Using a stand-alone simulation of Mini-TORCH with beam parameters taken from measurements made during the beam test, σ_{beam} is determined to range between 10 ps and 15 ps. The resolution of the time reference has been independently measured to have a value of 43 ± 3 ps.

Using data from the June 2018 beam test, sixteen measurements of σ_{TORCH} are made (with each measurement made for a different combination MCP column and incident particle species) which range between 83.6 ± 1.6 ps and 110.6 ± 1.6 ps.

Analysis of the most recent test-beam data is underway, and Fig. 6 shows the pattern observed with the beam impinging 175 mm below the top of the radiator plate and 5 mm to the side of the vertical edge closest to the MCP detectors. Using these data, a new estimate of the single photon timing resolution will be made, in addition to determining photon counting efficiency of the Proto-TORCH module.

3 Simulating TORCH in LHCb

This section describes the simulation of the TORCH detector in the LHCb software framework [10–13]. It also describes the implementation and performance of the TORCH pattern recognition algorithms on fully simulated events.

3.1 Detector geometry

In the Monte Carlo simulation, TORCH is placed in front of RICH2 at $z \approx 9500$ mm. In order to accommodate the detector, the position of RICH2 has been shifted along the beam line in z by 200 mm. Each module can be treated as a standalone detector and comprises a 660 mm × 2500 mm × 10 mm quartz radiator bar, a quartz focusing block and
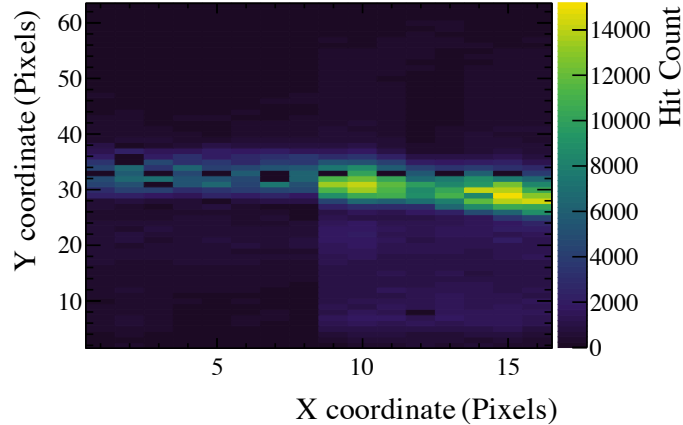
Figure 6: A hitmap of raw hits detected with two MCPs using the Proto-TORCH module. The data were taken with the beam striking 175 mm below the top of the radiator plate and 5 mm from the edge below the MCP detectors. The row of unoccupied pixels corresponds to channels used to inject a time reference into Proto-TORCH.

11 MCP-PMTs. The modules are separated from each other by a 20 mm air gap and are each surrounded by a 500 µm aluminium box. This allows the radiator bars to be optically separated in the simulation, such that each radiator bar can be reconstructed independently. The central radiator bar of each half is offset in y from the x-axis by 170 mm to allow room for the LHCb beam pipe. The other radiator bars are offset by 20 mm from the axis. In the discussion below, the modules above the beam pipe are labelled in increasing x from 1 to 9. The modules below the beam pipe are labelled from 10 to 18. Modules 5 and 14 are the central most modules and are exposed to the highest particle fluences.

Cherenkov photons produced in the radiator bar are transported to the periphery of the detector by total internal reflection at the quartz-air boundary. The photons are then focused in the $y - z$ plane onto the detector plane by a cylindrical mirror, with a radius of curvature of 260 mm. The focusing block is a quartz bar with the same extent in x as the radiator plate. The top and bottom of the focusing block are blackened to limit the possible paths from the top of the radiator plate to the detector plane. The sides of the block are not blackened, allowing for total internal reflection of photons from the boundary. The detector plane of each module is instrumented by eleven 60 mm × 60 mm MCP-PMTs with 53 mm × 53 mm active area. A visualisation of the TORCH detector components in the LHCb event display (`Panoramix`) is shown in Fig. 7. At present, the detector is free standing with no support structure. A holding frame for the bars will need to be simulated before a Technical Design Report is prepared.

The response of the MCP-PMTs is not simulated in GAUSS. Instead, the active area of the device is implemented in the simulation as a `GiGa` sensitive detector [14]. This records the true position, energy and arrival time of the photons, which are then stored at the output of GAUSS.

Figure 8 shows the additional material introduced by TORCH in front of the RICH2 detector. The 1 cm thick quartz bars correspond to 0.081 radiation lengths of material. Without a support structure, the majority of the material is outside the acceptance of the
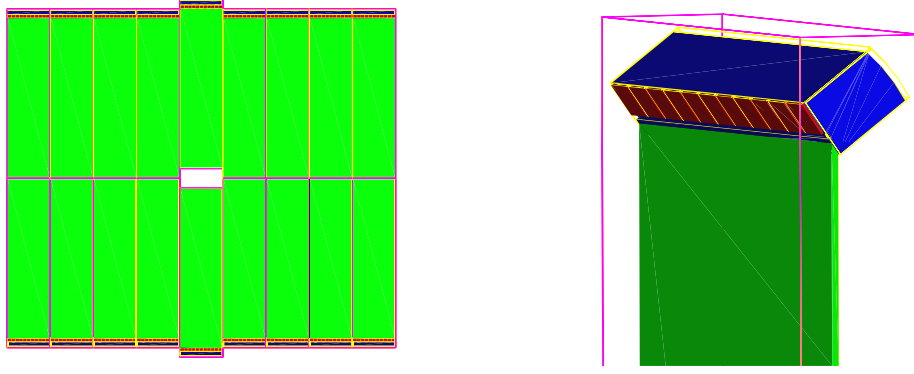
Figure 7: The TORCH geometry visualised in `Panoramix` showing (left) the TORCH detector view in the $x - y$ plane and (right) a close up view of a single module. The green bars are the TORCH radiator plate, the blue block is the focusing block and the red boxes represent the MCP-PMT detectors with their active area.

LHCb detector.
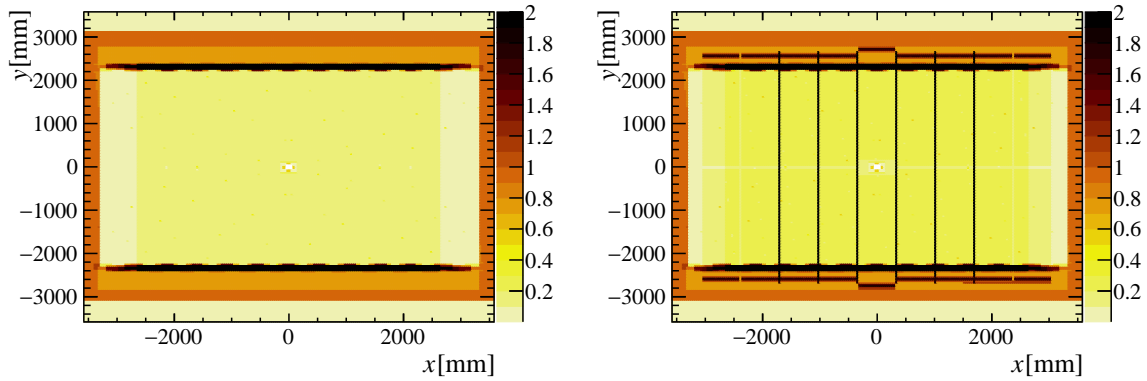
Figure 8: Material in terms of radiation length from the start of the Fibre Tracker to entry to the RICH2 volume without TORCH (left) and with TORCH (right). The vertical regions comprising a large number of radiation lengths correspond to particles passing all the way through the side of the 500 μm aluminium box. This situation does not occur for real charged particles in LHCb.

3.2 Simulation

The simulation of Cherenkov radiation in GEANT4 is handled by the `G4CherenkovProcess`. Charged particles with

$$\beta > \frac{1}{n(E_\gamma)} \tag{2}$$

produce Cherenkov photons in a cone with a uniform azimuthal angle and fixed polar angle (the Cherenkov angle)

$$\cos \theta_c = \frac{1}{\beta \, n(E_\gamma)} \tag{3}$$

7

about the particle direction, where E_γ is the photon energy and $n(E_\gamma)$ is the phase refractive index of the material. The Cherenkov yield for a particle of charge q in the material is given by

$$\frac{\mathrm{d}^2 N}{\mathrm{d}E_\gamma \mathrm{d}r} = \frac{\alpha}{\hbar c} q^2 \sin^2 \theta_c \ , \tag{4}$$

where r is the path length of the charged particle in the radiator. To save computation time in the ray-tracing of the photons within GAUSS, the photon-yield is down-scaled to 20% of its original value. This removes photons that would anyway not be observable due to instrumental inefficiencies, *i.e.* charge-collection efficiency, MCP-PMT quantum efficiency *etc.*. Photons are also only simulated in the energy range 1.5–7.0 eV.

The propagation of the Cherenkov photons to the detector plane is handled by GEANT4. The reflection of photons from the optical surfaces is handled by the `G4OpBoundaryProcess`. Cherenkov photons are reflected from the quartz-air boundary only if they satisfy total internal reflection requirements. The speed of the photons in the quartz is set by the group velocity of the material,

$$v_\mathrm{g} = c \left/ \left(n + E_\gamma \frac{\partial n}{\partial E_\gamma} \right) \right. \ . \tag{5}$$

The energy dependence of the group and phase velocities of photons within the radiator bar are shown in Fig. 9.
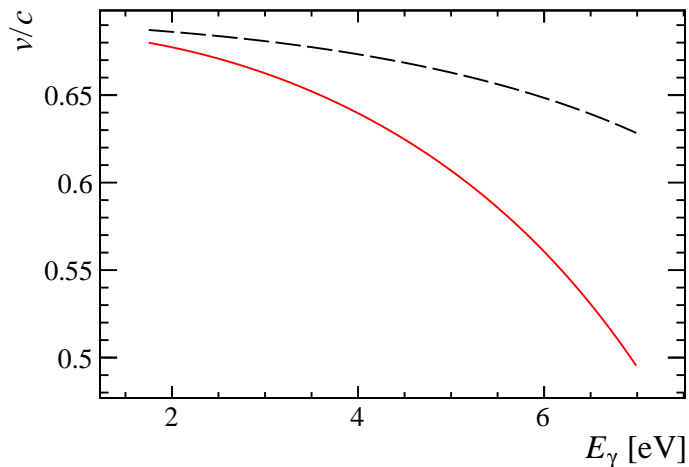
Figure 9: Group (red) and phase (dashed-black) velocity of optical photons in the quartz radiator bar.

Optical photons can be scattered by two mechanisms within the radiator bar and the focusing block: Rayleigh scattering and surface roughness of the quartz surface. Rayleigh scattering is simulated by `G4OpRayleigh` within GEANT4. The impact of Rayleigh scattering is negligible across the accessible energy range. The scattering due to surface roughness is modelled inside `G4OpBoundaryProcess` assuming the surface is smooth to the level of $\lambda_\mathrm{r} = 0.5$ nm. The probability for a photon to not undergo a Lambertian scatter is

$$\exp\left(-\left(4\pi \frac{\lambda_\mathrm{r}}{\lambda_\gamma} n(E_\gamma) \cos \theta_s \right)^2 \right) \ , \tag{6}$$

8

where θ_s is the angle of the photon with respect to the surface normal and λ_γ is the photon wavelength.

The final step of the simulation is to accept-reject the optical photons based on: the transmission of the glue (Epotek 305) at the interface between the radiator bar and the focusing block; the reflectivity of the cylindrical focusing mirror; the quantum efficiency and charge collection efficiency of the MCP-PMT. The glue is implemented as an optical cut rather than a layer in the simulation. This omits the effects of Fresnel reflection at the boundary. The efficiency of these different contributions as a function of the photon energy is shown in Fig. 10. Finally, the arrival time of the photons is smeared by 55 ps to account for the resolution (after charge sharing) of the detector electronics.
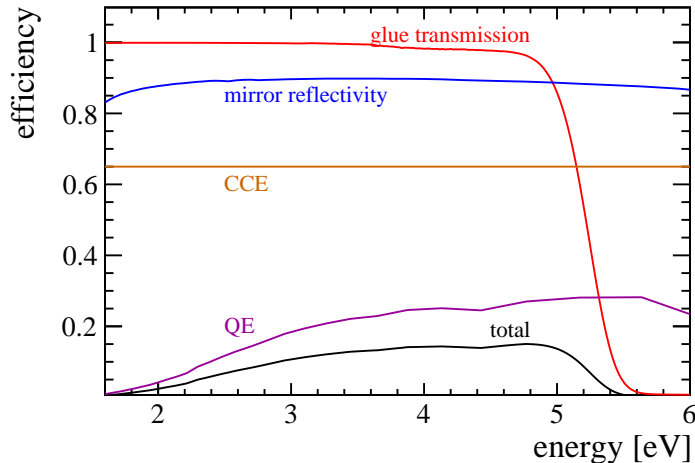

Figure 10: Optical efficiency of the TORCH system as a function of the photon energy. The individual contributions from the glue transmission, mirror reflectivity and the MCP-PMT charge-collection and quantum efficiencies are shown for reference.

The default upgrade simulation is used for all other detectors, with the exception that the position of RICH2 is offset compared to its nominal position.

3.3 Data taking conditions

The performance of the TORCH detector is studied under Upgrade Ib data-taking conditions using fully simulated $b\bar{b}$ events and a mean of 7.6 interactions per bunch-crossing. This corresponds to an instantaneous luminosity of $2 \times 10^{33} \, \mathrm{cm}^2 \, \mathrm{s}^{-1}$. The simulation also includes spill-over from the two proceeding and two following bunch-crossings. The spread of the pp interaction point in time and position along the beam axis (LHCb z-coordinate) is shown in Fig. 11. The typical spread in time of the interaction vertices is 210 ps.

3.4 Track reconstruction and extrapolation

The performance of TORCH is studied on long-tracks that can be reconstructed in the LHCb upgrade environment. The reconstructed tracks are extrapolated to the entrance of the TORCH radiator. Their path length between production vertex and TORCH entry point is calculated from the states on the track using a cubic spline interpolation. A
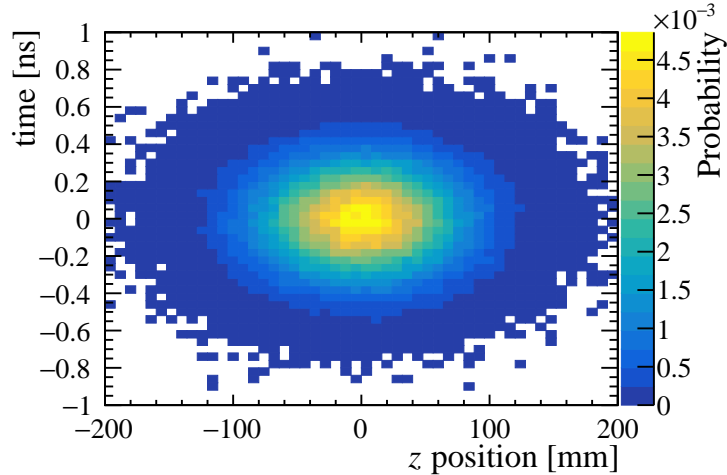
Figure 11: Distribution of simulated primary vertices in time and position along the beam line.

comparison between the reconstructed and true track entry positions and path-length in the simulation is shown in Fig. 12. The resolution is better in the bending plane than the non-bending plane due to orientation of the fibres in the Fibre Tracker. The resolution on the path-length is negligible compared to the total path-length of the particles.
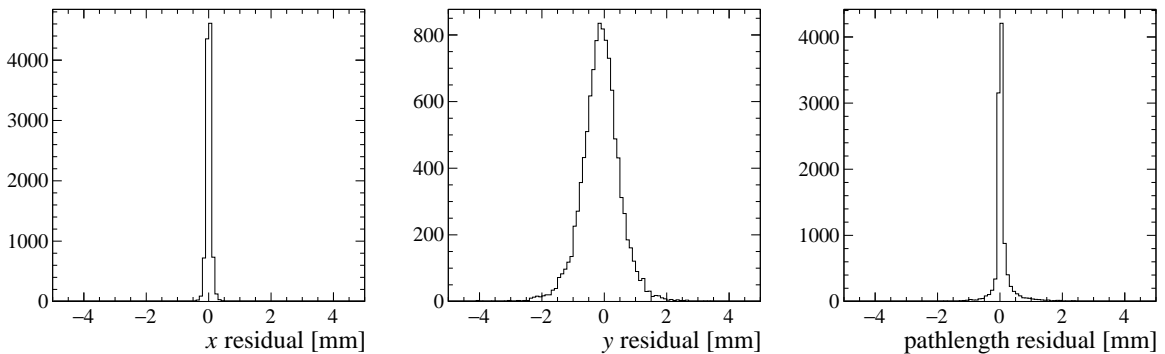
Figure 12: Comparison (left and centre) of the true and reconstructed entry position of charged particles entering the TORCH radiator bar and (right) of the path-length of the particle in the detector.

3.5 Event reconstruction

For each track, the log-likelihood for each considered hypothesis, h, is computed from

$$\log \mathcal{L}_h = \sum_{\text{hits}} \log P(\vec{x}_{\text{hit}}, t_{\text{hit}}, h). \tag{7}$$

The background contribution to the probability density function is assumed to be flat across the detector plane and is assumed to be uniform in time. This could be improved in future iterations of the algorithm. A global approach, like the one used in the RICH detectors, where all tracks are considered simultaneously could also be explored.

10

The probability density function for the signal on the detector plane is determined by simulating the passage of 10^6 photons per-track through the TORCH optics. Photons are generated uniform in azimuthal angle about the reconstructed track direction. The photon energy is sampled from Eq. 4, after accounting for the energy-dependent efficiency of the mirror, glue and MCP-PMT. The photon energy specifies the Cherenkov angle and, with the track direction and azimuthal angle, the subsequent direction of the photon in the radiator bar.

The position of the photon on the detector plane and its path length in the detector can then be computed without the need to ray-trace photons through the bar. The process involves the evaluation of only a small number of CPU intensive mathematical functions and takes $\mathcal{O}(0.1\,\mathrm{s})$ per track. Further improvements are expected with some code optimisation.

The expected total arrival time of the photon on the detector plane is calculated from

$$t_d = t_0 + \frac{r_{\mathrm{track}}}{\beta c} + \frac{r_\gamma}{v_{\mathrm{g}}} \ . \tag{8}$$

Here, t_0 is the production time of the charged track, r_{track} is the path length of the track from its production point to the photon emission point and r_γ is the path length of the photon in TORCH. The arrival time is then smeared by the same $55\,\mathrm{ps}$ resolution as the fully simulated photons. The value of t_0 is taken from the simulation and is assumed to be known perfectly. In practice this would need to be determined from the data (see Sec. 5.1).

3.6 Detector occupancy

The number of photons arriving per nanosecond on the detector plane in the Upgrade Ib data taking conditions is illustrated in Fig. 13. Photons produced by charged particles passing through the focusing block have been removed. It is assumed that additional shielding can be installed, outside the detector acceptance, in order to suppress this background. The $25\,\mathrm{ns}$ bunch-structure is clearly visible in Fig. 13. The signal in TORCH appears about $40\,\mathrm{ns}$ after the bunch-crossing, corresponding to the time-of-flight of particles with β close to one, plus the time-of-propagation inside the TORCH radiator. The signal bunch-crossing time corresponds to a t_0 of $0\,\mathrm{ns}$. The two preceding bunch crossings having crossing times at -50 and $-25\,\mathrm{ns}$. The two following bunch crossings have crossing times at $+25\,\mathrm{ns}$ and $+50\,\mathrm{ns}$.

The majority of the light-yield in Fig. 13 is not associated to reconstructed tracks. It is instead produced by secondaries entering the quartz radiator, for example from electron-positron pairs produced in photon conversions in the quartz bar.

The per-pixel occupancy for modules in the centre and near the side of the quartz plane is shown in Fig. 14.

3.7 Particle identification performance

The performance of the particle identification algorithm integrated over the full TORCH detector is shown in Fig. 15. TORCH is able to distinguish pions and kaons with momentum in the range 2–$10\,\mathrm{GeV}/c$ and protons from lighter particles up to $20\,\mathrm{GeV}/c$.
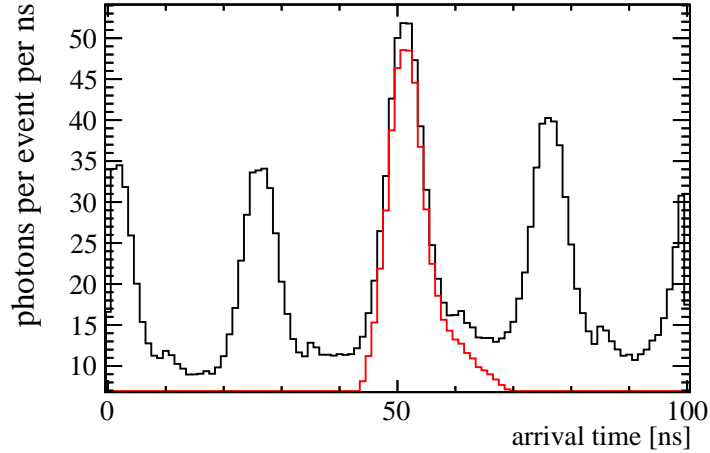
Figure 13: Photons arriving on the detector plane per nanosecond. The photons from the bunch-crossing containing the simulated $b\bar{b}$ event are shown in red.
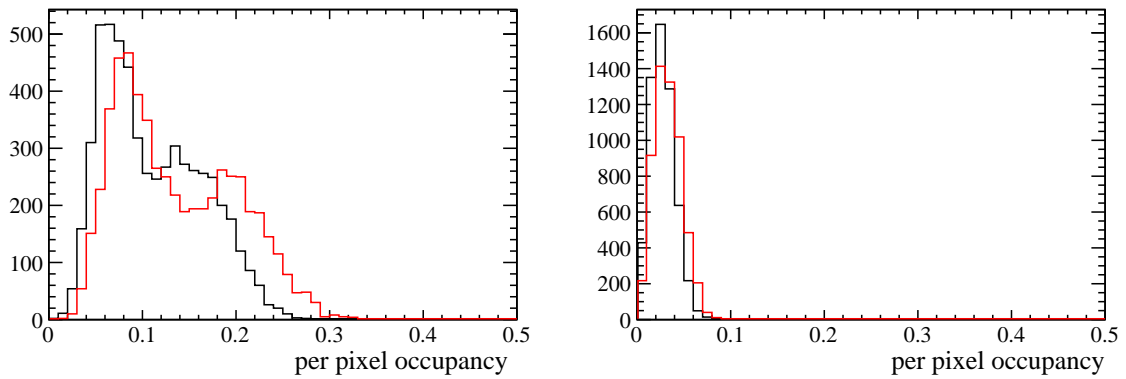

Figure 14: The per-pixel occupancy in 25 ns window for MCP-PMTs in (left) module 5 and (right) module 2. The red distribution shows the impact of charge-sharing between pixels.

At the time of writing these studies are still on going. Potential improvements in performance will be investigated, for example by changing parameters such as the granularity of the MCP-PMTs or by changing the reconstruction algorithm to a global likelihood.

4 Physics studies

The TORCH detector will improve the identification of low momentum particles to complement the existing discrimination provided by the RICH detectors. The advantages of TORCH will therefore be greater for processes that result in low momentum hadrons. The analysis to identify and quantify potential gains has been split into two sections: first, the impact on flavour tagging algorithms is discussed in Section 4.2; and second, the impact on specific decays involving kaons and protons in the final-state in Section 4.3. These results are preliminary and subject to further improvements.
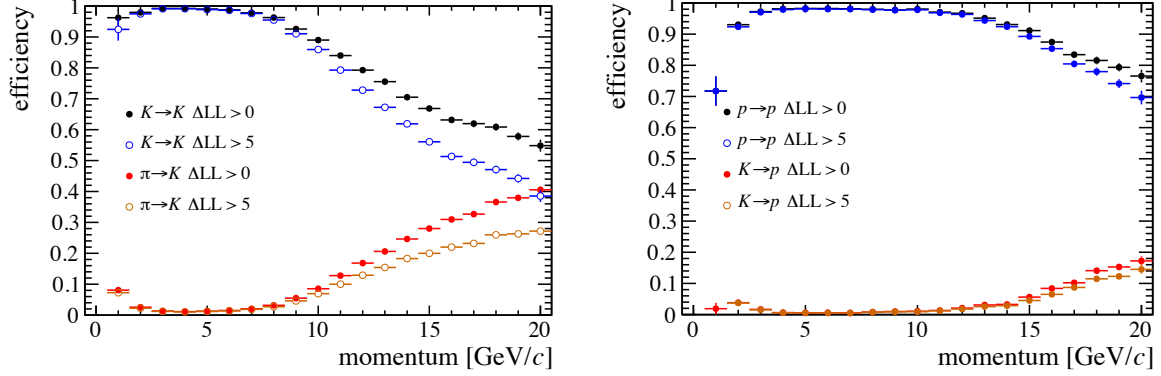
Figure 15: Particle identification performance of TORCH in the momentum range 2–20 GeV/c at a luminosity of $2 \times 10^{33}\,\text{cm}^{-2}\,\text{s}^{-1}$. (Left) The pion-kaon separation and (right) proton-kaon separation integrated over the full TORCH detector when modelled in the full LHCb Monte Carlo framework.

4.1 Particle identification performance

The TORCH PID performances detailed in Section 3.7 are used to quantify improvements. For the studies of flavour tagging and specific decay modes in this section, the PID performance is applied to reconstructed particles in centrally-produced LHCb simulation samples for each of the decay modes, generated for the Upgrade Ib conditions ($\mathcal{L} = 2 \times 10^{33}\,\text{cm}^{-2}\,\text{s}^{-1}$).

4.2 Tagging

Flavour tagging algorithms are used to determine the flavour of neutral mesons at their production. This is a crucial component of time-dependent measurements of CP asymmetries, see for example Ref. [15]. The algorithms exploit information in $pp \to b\bar{b}X$ events that can be correlated to the flavour of the b-hadron at production. The algorithms are split into two classes: same side (SS) and opposite side (OS) taggers. The SS algorithms identify particles produced in the hadronisation of the b-quark associated to the b-hadron candidate. The OS algorithms identify particles associated to the decay of the other b-quark in the event, *i.e.* the one that doesn't form part of the b-hadron candidate. In both cases, the charge of the associated particle is correlated to the initial flavour of the b-hadron candidate.

4.2.1 Relevant tagging algorithms

Tagging algorithms require identifying the species of the associated flavour tagging particle, with the OSKaon, SSKaon, and SSProton algorithms [16–18] being of particular relevance to TORCH due to the potential of improvement in the identification of kaons and protons. The SSPion algorithm is not expected to gain significantly from the improved PID because, although the rate of kaons and protons misidentified as pions may be reduced by TORCH, the dominance of the number of pions in an event limits the benefit.

The SSKaon algorithm selects charged kaon candidates that could have been produced from the hadronisation of the $\bar{s}$-quark associated to the production of a B_s^0 meson ($\bar{b}s$).
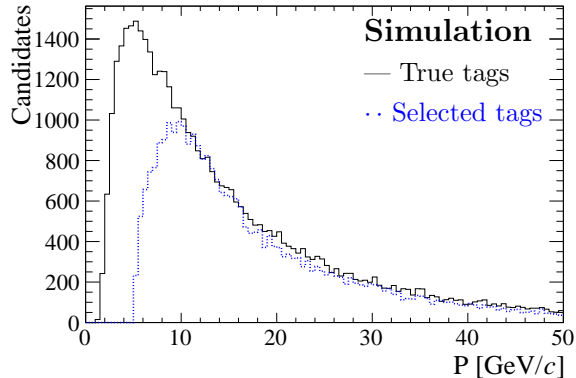
Figure 16: The momentum distribution of truth-matched (black) and selected (blue) tags for the `SSKaon` algorithm. The selected tags must pass the nominal LHCb PID and momentum requirements as described in Section 4.2.2.

Therefore, a positively charged kaon, a K^+ ($u\bar{s}$), indicates the flavour at production was a B_s^0, and a K^- indicates a $\overline{B}_s^0$. The truth-matched momentum distribution for these tagging particles in Monte Carlo simulations are shown in Fig. 16 in black. A large fraction of tags have a momentum in the range that could potentially benefit from TORCH PID, as they are currently not selected using the nominal selection, shown in blue.

The `OSKaon` algorithm selects hadrons produced in the decay of the other b-hadron in an event. In contrast to the SS algorithms, these tags are not consistent with originating from the primary interaction vertex as they are produced at secondary vertices. Therefore, in addition to particle identification, it is important to correctly associate the track to the correct primary vertex to accurately determine the b-hadron flavour. As the number of pile-up interactions increases, it becomes more difficult to correctly associate the track to the primary interaction, therefore the performance of these algorithms decreases.

Studies by the flavour tagging group have shown that the performance of the state-of-the-art tagging algorithms decrease as the number of primary interactions increases [3]. Additionally the same trend is observed as a function of the number of tracks in the detector. Therefore, it is of great interest to identify ways of mitigating this performance loss.

The sensitivity of measurements that rely on flavour tagging can be quantified using the effective tagging power $\epsilon_{\text{eff}} = \epsilon_{\text{tag}} \times (1 - 2\omega)^2$, where ϵ_{tag} is the probability that a given b-hadron candidate has an appropriate tag, and ω is the fraction of tagged candidates that are incorrectly tagged.

4.2.2 Incorporation of TORCH PID performance

The effect of the TORCH PID efficiencies on the tagging performance is studied using simple cut-based tagging algorithms, based closely on previous versions of current tagging software [16, 17]. More recent approaches to tagging in LHCb exploit multivariate analysis techniques, however, the use of cut-based algorithms is expected to isolate the improvement that TORCH itself provides, without the need for extensive re-optimisation of the full framework. The following procedure is employed:

1. A loop is performed over the container of `Long` tracks in events with a candidate B

meson (`StdAllNoPIDsKaons`).

2. Tracks with a momentum above $10\,\mathrm{GeV}/c$ are selected if they pass 'nominal' tagging-algorithm selection requirements, defined below.

3. For tracks below $10\,\mathrm{GeV}/c$ three different selections are considered:

    (a) *The nominal selection*, where the existing momentum, p_T, and LHCb PID cuts are applied as a baseline;

    (b) *The perfect PID selection*, a sample in which the MC truth information is used to only select the correct species (*e.g.* kaons);

    (c) *The TORCH selection*, a sample in which tracks identified by MC truth information to be protons, pions or kaons are retained according to the relevant TORCH PID efficiency or mis-identification rate as determined from the stand-alone TORCH simulations;

4. If any of the strategies result in more than one tag candidate, the one with the highest p_T is chosen.

The charge of the chosen tag is compared to the MC truth information of the b-hadron initial flavour to determine whether the tagging decision is correct. The *perfect PID* category is used to set an upper limit of the possible improvement in the tagging performance. This method has been constructed to simplify the comparison of the different tagging configurations. Therefore the performance of these algorithms are suboptimal compared to the state-of-the-art methods. Additionally, these algorithms provide no prediction of the mistag rate which further limits their performance. The selection requirements implemented in these simple tagging algorithms are detailed in Table 1.

The performance of the `SSKaon` algorithm is studied using a sample of simulated $B_s^0 \to D_s^+\pi^-$ decays, whilst the `OSKaon` performance can be determined using both the $B_s^0 \to D_s^+\pi^-$ and a $B^+ \to J/\psi K^+$ sample. The effective tagging power for each of the three selections are listed in Table 2. Both the `SSKaon` and `OSKaon` tagging algorithms show significantly higher effective tagging powers when the stand-alone TORCH simulation PID performance is included. The improvement is independent of the sample considered for the `OSKaon` algorithm. Performance increases of between 20–30% are observed.

4.2.3 Incorporation of timing information

The TORCH detector is expected to determine a track's time of arrival to a precision of around $15\,\mathrm{ps}$. In a high pile-up environment, this timing information may help to disentangle from which primary interaction the track originated. The deterioration of the tagging performance as a function of the number of PVs and tracks in an event could be alleviated with this extra information. Presently, the TORCH simulation does not model the per-track timing information, therefore to determine the upper limit of any improvement in tagging the following procedure is used:

1. Various relevant opposite-side algorithms are developed using cut-based selections;

2. The samples are selected twice, once with the nominal selection and a second time using the MC truth information to exclude all tracks that originated from a different PV to the signal candidate;

Variable	SSKaon		OSKaon	
	Nominal	TORCH	Nominal	TORCH
p	>5250 MeV/c	>2000 MeV/c	>2000 MeV/c	>2000 MeV/c
p_{T}	>850 MeV/c	>200 MeV/c	>200 MeV/c	>700 MeV/c
PIDK	>3.5	>15.0	>3.5	>30.0
PIDp−PIDK	<8.5	<-5.0	<8.5	<10.0
χ^2_{IP}	< 4.125		> 31.0	
IP			< 1.6	
$\Delta\phi$	< 0.825			
$\Delta\eta$	< 0.6			
ΔR	< 10			
$m(BK) - m(B)$	< 1850 MeV/c^2			
PU χ^2_{IP}	> 3.0		> 31.0	
Dist phi	> 0.005		> 0.005	
χ^2_{Trk}	< 3.0		< 3.0	
Ghost Prob.	< 0.35		< 0.35	

Table 1: Selection requirements used for each of the simple tagging algorithms. The variables PIDK and PIDp refer to the difference in the log-likelikood of the kaon and pion, or proton and pion hypotheses in either the simulation of the Upgrade Ib RICH detectors (nominal), or from the TORCH stand-alone performance (TORCH). The variables IP and χ^2_{IP} are the impact parameter and difference in the best primary vertex fit χ^2 with and without the tag track included. The best primary vertex is the one to which the candidate has the smallest χ^2_{IP}. The variables $\Delta\phi$, $\Delta\eta$ and ΔR describe the difference in direction of the candidate and tag track in the azimuthal angle, pseudo-rapidity, and in their combination $\Delta R = \sqrt{\Delta\phi^2 + \Delta\eta^2}$. The quantity $m(BK) - m(B)$ is the difference between the invariant mass of the candidate and tagging track and the invariant mass of just the candidate. PU χ^2_{IP} is the value of χ^2_{IP} for the second best primary interaction vertex, $i.e.$ a pile up (PU) vertex. Dist phi helps remove cloned tracks by comparing the angle between all candidate tracks and the tag. The quantity χ^2_{Trk} describes the quality of the track fit, and Ghost Prob helps discriminate against ghost tracks.

3. The performance is compared to show the best possible improvement if TORCH could perfectly associate tracks to PVs.

The two OS tagging algorithms developed for this study are OSKaon and OSMuon algorithms. For the OSKaon algorithm, the selection is the same as the nominal configuration previously described in Table 1. The selection of the OSMuon algorithm is detailed in Table 3 [16].

The tagging power is studied as a function of the number of primary interactions and number of tracks in an event and is shown for both OS algorithms in Fig. 17. It can be seen that by removing all tracks from other primary interactions the performance improves. The relative performance gain is generally larger at higher values of N_{PV}. The dependence of the tagging power on N_{PV} and N_{Tracks} is not completely eliminated by artificially removing these incorrect tracks from the tagging algorithm. This may imply the overall occupancy of the detector still degrades the performance. The improvement shown in Fig. 17 is an upper limit of the improvement that the TORCH timing information alone could provide to tagging ($i.e.$ this is independent of any improvement in PID discrimination). In future,

Tagger	$B_s^0 \to D_s^+ \pi^-$		
	Nominal	TORCH	Perfect
SSKaon	$1.20 \pm 0.05\%$	$1.52 \pm 0.05\%$	$1.61 \pm 0.05\%$
OSKaon	$1.29 \pm 0.05\%$	$1.73 \pm 0.06\%$	$1.80 \pm 0.06\%$

Tagger	$B^+ \to J/\psi\, K^+$		
	Nominal	TORCH	Perfect
OSKaon	$1.06 \pm 0.04\%$	$1.51 \pm 0.05\%$	$1.61 \pm 0.05\%$

Table 2: Effective tagging power ϵ_{eff}, for the different tagging configurations when studied using simulated samples of $B_s^0 \to D_s^+ \pi^-$ and $B^+ \to J/\psi\, K^+$ decays. The three scenarios modify the selection of tagging tracks with momentum less than $10\,\text{GeV}/c$.

Variable	OSMuon
p_{T}	$>1100\,\text{MeV}/c$
χ^2_{IP}	> 0.0
PU χ^2_{IP}	> 3.0
Dist phi	> 0.005
χ^2_{Trk}	< 3.0
Ghost Prob.	< 0.4
PIDmu	> 3.0
ProbNNmu	> 0.35
ProbNNk	< 0.8
ProbNNe	< 0.8
ProbNNpi	< 0.8
ProbNNp	< 0.8

Table 3: Selection requirements used for the simple OSMuon tagging algorithm. The *ProbNN* variables are neural-network based PID variables.

more complete simulations that could model the timing information of the individual tracks will provide a more realistic picture.

4.3   Improvements for specific channels

A range of physics analyses would gain from the improved low momentum PID efficiency provided by TORCH. For these preliminary studies, a focus has been placed on 'benchmark' modes involving protons in the final-state and modes where significant gains are expected by improving $K - \pi$ separation in the GeV/c momentum range.
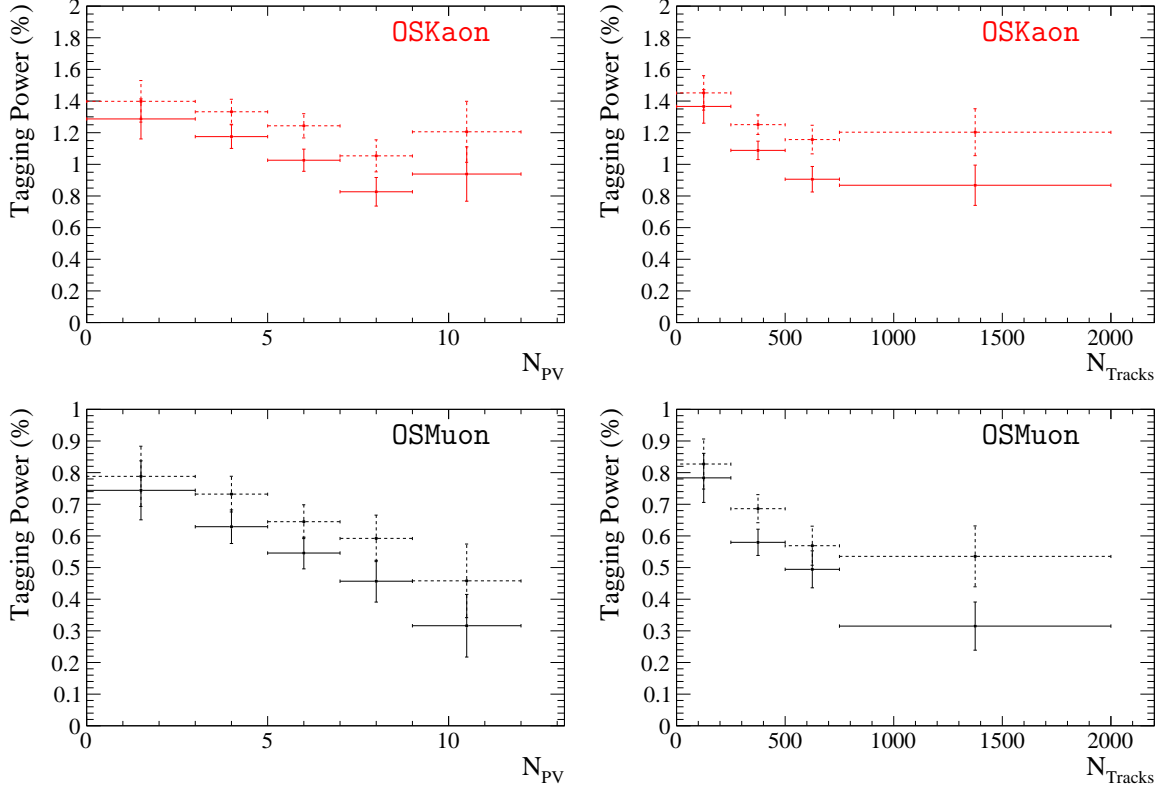
Figure 17: The effective tagging power as function of (left) the number of primary interactions and (right) tracks in an event. The nominal performance is represented by filled markers and the potential performance when tracks from other primary interactions are removed is represented by dashed markers. This performance is evaluated on a sample of $B^+ \to J/\psi K^+$ decays.

4.3.1 The decay $\Lambda_b^0 \to J/\psi\, pK^-$

The decay $\Lambda_b^0 \to J/\psi\, pK^-$ has been of great interest since the observation of $J/\psi\, p$ resonances consistent with pentaquark states by LHCb in 2015 [19]. The selection of this mode requires placing tight PID requirements on the proton and kaons to prevent contamination from mis-identification backgrounds. For the kaon this correspond to DLL$(K - \pi) > 0$ and DLL$(p - K) < 3$, and for the proton DLL$(p - \pi) > 10$ and DLL$(p - K) > 3$. For this study, candidates are reconstructed using the same requirements as the published analysis [20], but comparing with and without any PID requirements applied. The momentum distribution of the protons and kaons can be seen in Fig. 18 both without any requirements on the PID variables, labelled 'perfect PID' (red), and with the LHCb PID requirements applied (blue). It can be seen that the low momentum particles are particularly affected by the PID requirements. To incorporate the expected TORCH PID performance, the RICH proton and kaon PID efficiency is parametrised as a function of momentum. This is then combined with the TORCH PID efficiency for the same DLL cut values as obtained from the TORCH simulations detailed in Section 3.7. The two efficiencies are combined by selecting whichever is greater at a given momentum. This may be an underestimate of the potential improvement if the TORCH detector selects a different subset of tracks to the RICH detectors. The momentum distribution multiplied by the combined efficiency is also shown in Fig. 18 in red. The addition of
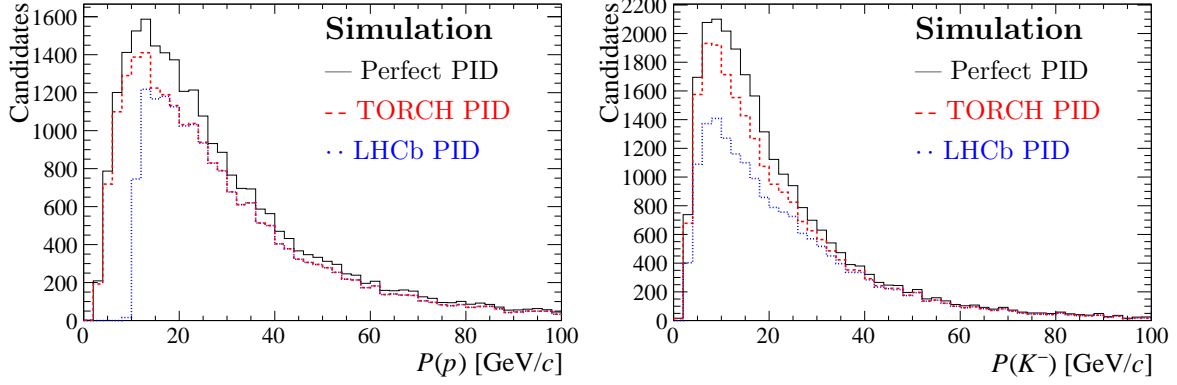
18

Figure 18: The momentum distribution of protons (left) and kaons (right) in simulated $\Lambda_b^0 \to J/\psi p K^-$ decays. The distribution is shown without PID requirements (black), with the nominal LHCb PID requirements (blue) and with the additional performance provided by TORCH (red).
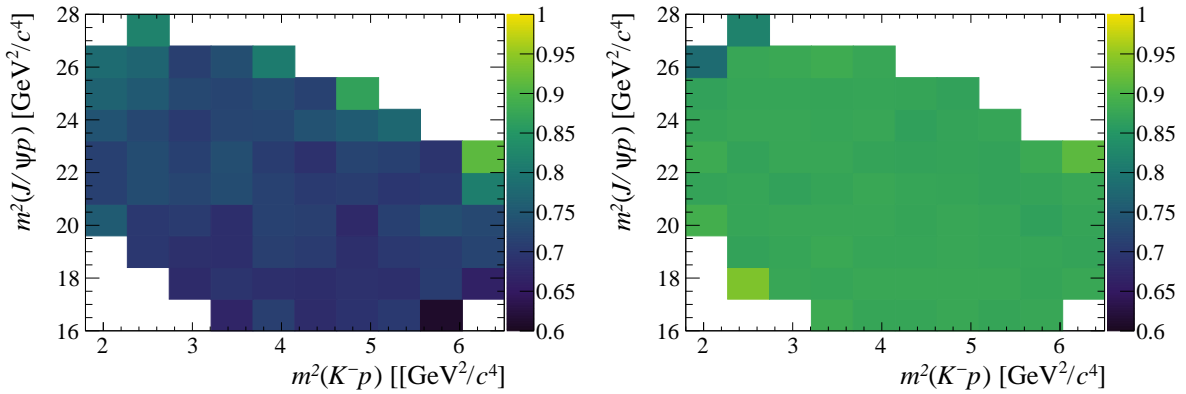

Figure 19: The Dalitz plot distribution of $\Lambda_b^0 \to J/\psi p K^-$ decays selected with the nominal LHCb PID requirements (left) and with the additional performance of the TORCH detector (right).

TORCH increases the size of the signal yield by around 23% with respect to the RICH PID selection requirements.

In addition to increasing the total size of the yield, improving the low momentum PID performance may reduce efficiency variation as a function of other quantities that are related to momentum. The analysis of $\Lambda_b^0 \to J/\psi p K^-$ decays involves studying the distribution of the data as a function of the Dalitz plot variables $m^2(J/\psi p)$ and $m^2(K^- p)$. Applying the nominal PID requirements leads to an efficiency that varies as a function of these variables as shown in Fig. 19. When the improved low momentum PID performance provided by TORCH is included, the efficiency becomes significantly more uniform as a function of the Dalitz plot coordinates. This may help to reduce systematic uncertainty in amplitude analyses of this mode.

A qualitative study is performed to investigate the improved TORCH mis-identification rates at low momentum by looking at the momentum distribution of existing Run II data samples. This data set was taken with the phase I LHCb detector and Run II luminosity , hence its study is only intended to be illustrative. The sample of data is reconstructed using the selection in the published analysis, but without any requirements placed on the PID
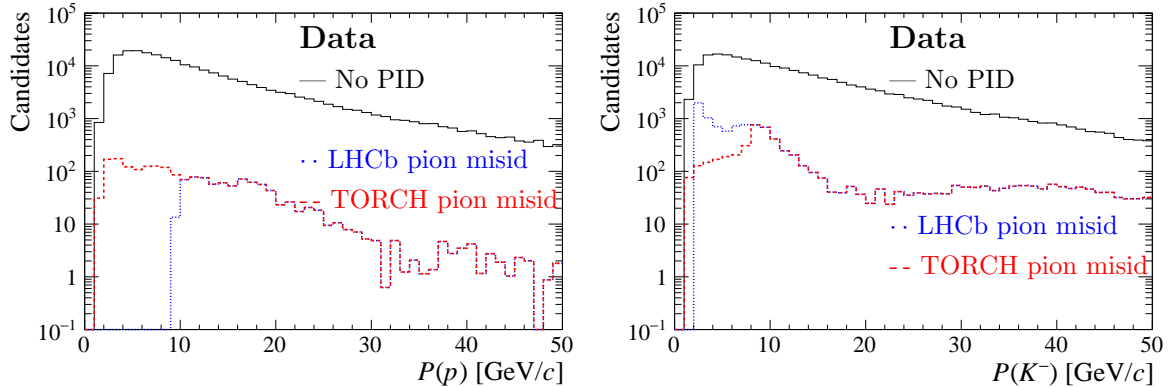
Figure 20: The distribution of combinatorial background candidates in a data sample of $\Lambda_b^0 \to J/\psi p K^-$ decays. The distribution is shown without any requirements places on the PID variables (black) and multiplied by the expected LHCb (blue) and TORCH (red) pion mis-identification efficiency distributions. This demonstrates the level of background remaining if the background were entirely composed of pions.

variables. A fit is performed to the invariant mass of the Λ_b^0 baryon and the combinatorial background is isolated using the *sWeight* procedure. The momentum distribution of the proton and kaon in this combinatorial background are shown in Fig. 20. The combinatorial background is assumed to be dominated by pions and therefore multiplied by the expected LHCb and TORCH pion-proton mis-identification rates for the relevant PID requirements. For the proton distribution, it can be seen that the LHCb mis-identification rate is zero below $10 \,\mathrm{GeV}/c$ as there is no positive proton identification (everything is called a pion or kaon, so there are no pions misidentified as protons). With the addition of TORCH the low momentum performance is comparable to high momentum. For the kaon distribution, the additional TORCH discrimination power is seen to reduce the low momentum background.

4.3.2   The decay $\Lambda_b^0 \to p\pi^-\pi^+\pi^-$

The first evidence for *CP* asymmetry in the baryon sector was observed in $\Lambda_b^0 \to p\pi^-\pi^+\pi^-$ decays in 2016 [21]. The selection of these decays requires applying PID requirements to identify the proton, as well as distinguishing the pions from other hadrons in crossfeed decays. The existing analysis places a requirement on the variable `ProbNNp` to remove backgrounds from 4- and 5-body b-hadron backgrounds. To allow a comparison with the expected TORCH performance, similar requirements of $\mathrm{DLL}(p-\pi) > 5$ and $\mathrm{DLL}(p-K) > 0$ are used for this study. The distribution of proton momentum with and without these PID requirements are shown in Fig. 21. Additionally, the momentum distribution of decays selected when the TORCH performance is incorporated as before is shown in red. This results in approximately 10% more signal.

An attempt to qualitatively investigate how TORCH might improve the removal of combinatorial background has been performed by looking at the momentum distribution of combinatorial background in real Run II data (Fig. 22). The momentum distribution is studied firstly without PID cuts applied, then subsequently assuming all background originates from pions and incorporating the TORCH pion-proton mis-identification efficiency. The stripping line for this decay has a requirement of ProbNNp > 0.05 placed on the proton which cannot be removed. Therefore to unfold the effect of this requirement,
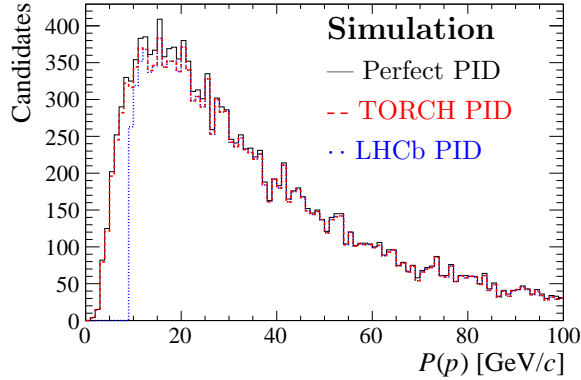
Figure 21: The proton momentum distribution in simulated $\Lambda_b^0 \to p\pi^-\pi^+\pi^-$ decays selected without any requirements placed on the PID variables (black), with LHCb PID requirements (blue) and with the addition of the TORCH performance (red).
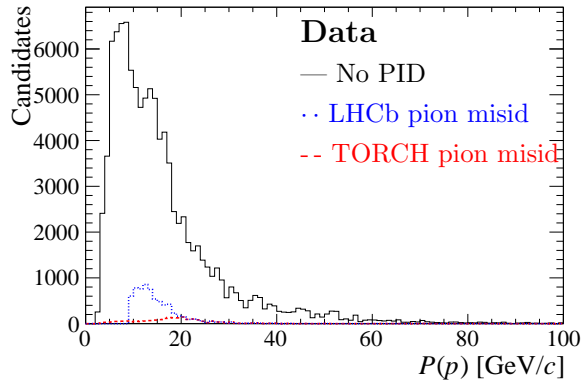

Figure 22: The momentum distribution of combinatorial background contributing to $\Lambda_b^0 \to p\pi^-\pi^+\pi^-$ decays in data selected without any requirements placed on PID variables (black) and the expected momentum distribution assuming the combinatorial background is composed entirely of pions using the LHCb mis-identification rate (blue) and TORCH mis-identification rate (red). The lack of positive proton identification with LHCb below $10\,\mathrm{GeV}/c$ results in the sharp cut off, as all hadrons are identified as pions.

the momentum distribution is first divided by the pion mis-identification efficiency for ProbNNp > 0.05 as obtained with `PIDCalib`, again assuming the distribution is dominated by pions. The momentum distribution combined with the TORCH mis-identification rate shows an improvement in background rejection over the LHCb distribution.

4.3.3 Semileptonic measurements of V_{ub}

The decay $\Lambda_b^0 \to p\mu^-\overline{\nu}_\mu$ can be used to perform a measurement of the CKM element V_{ub} and has been previously studied at LHCb [22]. To control backgrounds from mis-identified hadrons, the reconstruction of this decay employs the use of tight PID requirements on the proton. As a result of the poor proton-kaon separation at low momentum, currently only protons with $p > 15\,\mathrm{GeV}/c$ are considered. Therefore, any improvement that allows the region removed by this requirement to be included will improve the efficiency of the
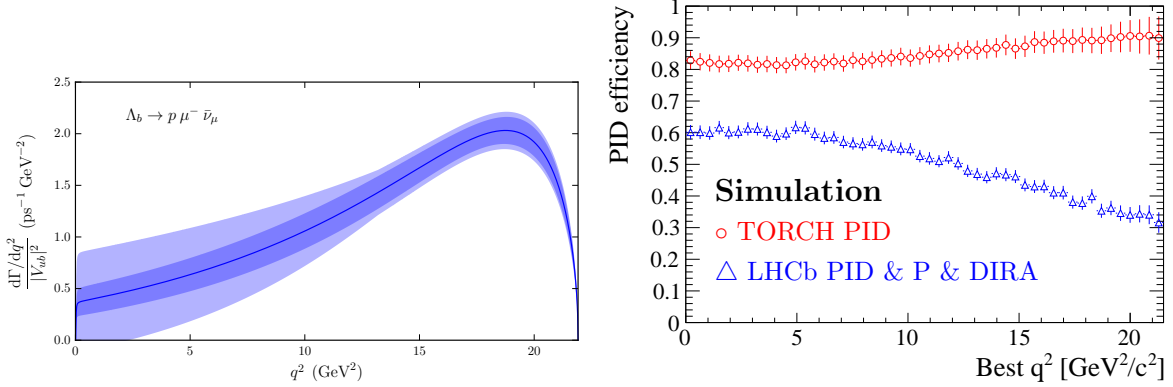
Figure 23: (Left) The theoretically calculated form factors required to measure V_{ub} as a function of q^2, taken from [23] and (right) the PID efficiency of $\Lambda_b^0 \to p\mu^-\overline{\nu}_\mu$ candidates as a function of q^2 using the existing requirements on LHCb PID variables, momentum and DIRA (blue) and with the addition of the TORCH PID performance, but with looser momentum and DIRA requirements as described in the text (red).

selection.

In order to measure the CKM element V_{ub}, input is needed from externally-calculated form factors. The uncertainty on these theoretical predictions vary as a function of $q^2 = m^2(\mu^-\overline{\nu}_\mu)$, the momentum transfer of the leptonic system. The values are more precisely predicted at high q^2 as shown in Fig. 23. At high values of momentum transfer, the momentum of the associated hadron is low, therefore the region in which the theoretical predictions are best known corresponds to low momentum protons.

A sample of $\Lambda_b^0 \to p\mu^-\overline{\nu}_\mu$ decays is reconstructed using the stripping selection defined in `StrippingLb2pMuNuVubLine`. However, the previous tight requirement on the proton momentum is now relaxed. Additionally this stripping line requires that direction angle (DIRA), defined to be the angle between the muon-proton vertex direction with respect to the PV and the muon-proton 4-momenta, has $\cos(\theta) > 0.9994$. This effectively requires the muon and proton to take most of the momentum, removing events with low momentum protons. These two conditions are relaxed to $P > 2\,\mathrm{GeV}/c$ and $\cos(\theta) > 0.994$ respectively.

The combined efficiency for selecting signal candidates, taking into account the additional TORCH PID performance, and relaxed momentum and DIRA requirements, is shown as a function of the reconstructed q^2 in Fig. 23. When calculating the reconstructed q^2, the missing neutrino momentum leads to two solutions. To minimise bin migration, the existing analysis requires that *both* q^2 solutions are above $15\,\mathrm{GeV}^2/c^2$ to reduce the uncertainty from the theoretical form factors. In this region, including the TORCH performance increases the signal yield by approximately 130%.

The decay $B_s^0 \to K^-\mu^+\nu_\mu$ can also be used to determine V_{ub}. The selection requires the use of tight PID requirements to suppress backgrounds from pions and protons. Although this mode has not yet been measured by LHCb, the selection of candidates would require a tight momentum cut to control the background levels. A simulation sample is reconstructed using the selection defined in `StrippingB2XuMuNuBs2KLine`, without the PID requirements ($\mathrm{DLL}(K - \pi) > 5$ and $\mathrm{DLL}(K - p) > 5$). The PID efficiency is investigated as a function of q^2 as shown in Fig. 24. The distribution is shown using the existing LHCb PID requirements, and incorporating the TORCH PID performance at low
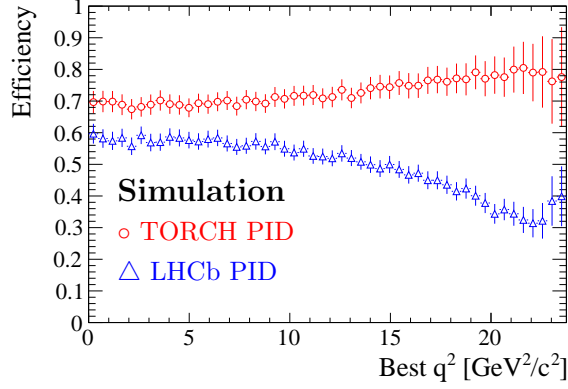
Figure 24: The PID efficiency of $B_s^0 \to K^- \mu^+ \nu_\mu$ candidates as a function of q^2 using the existing LHCb PID variables (blue) and with the addition of the TORCH PID performance (red).
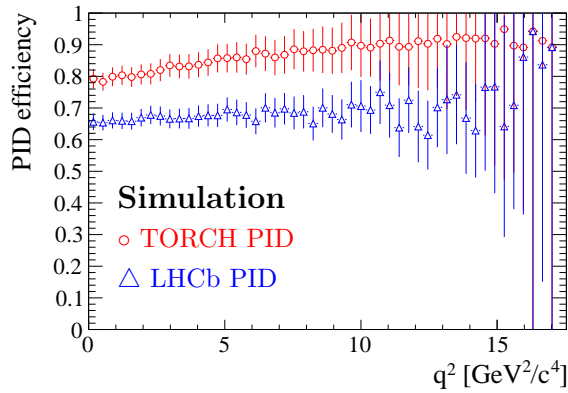

Figure 25: The selection efficiency of $\Lambda_b^0 \to pK^- \mu^+ \mu^-$ candidates as a function of $q^2 = m(\mu^+\mu^-)$ using the existing LHCb PID variables (blue) and with the addition of the TORCH PID performance (red).

momentum as described before. The TORCH PID performance improves the efficiency at high q^2. Across the whole q^2 range this corresponds to an increase in signal yield of 35%. If the range of q^2 was limited to higher values to reduce theoretical uncertainties, the improvement from TORCH would be greater, for example 54% for $q^2 > 10\,\text{GeV}^2/c^2$.

4.3.4 The decay $\Lambda_b^0 \to pK^- \mu^+ \mu^-$

The decay $\Lambda_b^0 \to pK^- \mu^+ \mu^-$ is a good candidate to gain from the improved performance TORCH offers. The presence of a proton and kaon necessitates PID cuts, and at high values of $m(\mu^+\mu^-)$ the momentum of these hadrons will be low. The candidates are selected using the line `StrippingB2XMuMu_Line` without any PID requirements. As the existing analysis uses requirements on `ProbNN` variables, similar requirements of $\text{DLL}(K-\pi) > 5$ and $\text{DLL}(K-p) > 0$ are employed. The distribution of the PID efficiency as a function of $m(\mu^+\mu^-)$ is shown in Fig. 25. Including TORCH leads to a increase in yield of 24% averaged across all q^2.
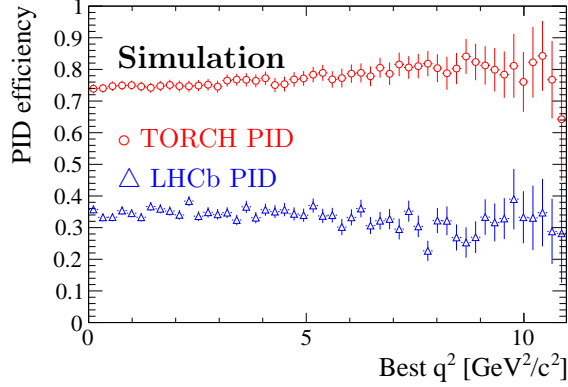
Figure 26: The PID efficiency of $B^+ \to p\bar{p}\mu^+\nu_\mu$ decays as a function of the reconstructed q^2. The distribution in blue represents the current efficiency of the combined momentum and PID selections, where as the points in red show the potential improvement from TORCH by removing the momentum requirements and improving the PID efficiency.

4.3.5   The decay $B^+ \to p\bar{p}\mu^+\nu_\mu$

The mode $B^+ \to p\bar{p}\mu^+\nu_\mu$ can be used to measure the ratio

$$R(p\bar{p}) = \frac{\mathcal{B}(B^+ \to p\bar{p}\tau^+\nu_\tau)}{\mathcal{B}(B^+ \to p\bar{p}\mu^+\nu_\mu)} \tag{9}$$

which can be used as a test of lepton flavour universality in the Standard Model. The presence of a proton and antiproton in the decay leads to difficulty in controlling misidentified backgrounds due to the poor PID performance at low momentum. Therefore in the selection of these decays the requirement $p > 18\,\mathrm{GeV}/c$ is placed on both protons. In addition to this, tight PID cuts of $\mathtt{DLL}(p-\pi) > 10$ and $\mathtt{DLL}(p-K) > 5$ are used. The combined efficiency of the momentum and PID requirement is shown in Fig. 26 as a function of the reconstructed momentum transfer q^2. With TORCH, the increase in signal yield is approximately 121%. It should be noted that the improvement depends on the distribution of $m(p\bar{p})$ found in data, as lower $m(p\bar{p})$ results in lower momentum hadrons, and therefore more to gain. This simulation sample is generated flat across phase space, whereas the data have been found to concentrate at low $m(p\bar{p})$, implying this yield increase may be even larger than predicted here.

4.3.6   Other modes

In general, analyses that place tight requirements on kaon-proton separation stand to benefit the most from the additional TORCH performance. However, a wide range of other analyses may be improved in a less direct manner. One example considered is the decay $B^0 \to DK^{*0}$, used to perform measurements of the CKM angle γ. This mode is currently statistically limited, so improving the signal efficiency can have a direct impact on the measurement precision. One way that TORCH may contribute is by reducing the level of double mis-identification polluting $K^{*0} \to K^-\pi^+$ decays. The large width of the K^{*0} resonance means a relatively tight mass window is required to control the double mis-identification background. Including the TORCH PID performance allows the
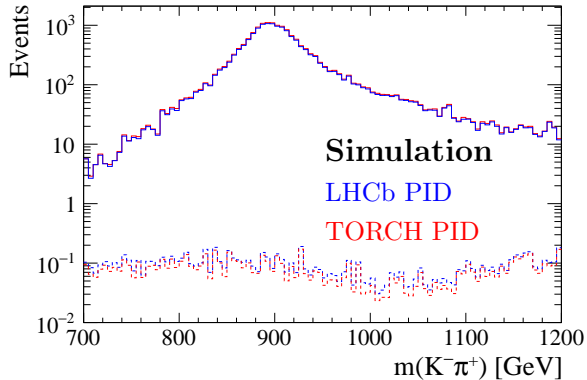
Figure 27: The mass distribution of correctly reconstructed $K^{*0} \rightarrow K^- \pi^+$ decays (filled lines) and the double mis-identification background (dotted lines). The efficiencies of each are shown with the LHCb PID requirements (blue) and with the addition of the TORCH performance (red).

window to be widened from $\pm 50.0 \, \text{MeV}/c^2$ to $\pm 54.0 \, \text{MeV}/c^2$ for the same level of double mis-identification. This increased the signal efficiency by 8% (Fig. 27).

5 Further studies

As previously stated, studies of the performance of TORCH at a luminosity of $1 \times 10^{34} \, \text{cm}^{-2} \, \text{s}^{-1}$ for Upgrade II initially indicate that, although there is some drop in performance with respect to Upgrade Ib, the kaon and proton efficiencies can be largely maintained. Work is ongoing to optimize these results as a function of the detector's parameters (granularity, focussing, backgrounds *etc.*). The physics studies will be further developed to incorporate the PID performance from the full description of TORCH in the LHCb simulation at both Upgrade Ib and Upgrade II luminosities in the coming weeks.

In addition to the above studies, the following areas have been identified for potential investigation.

5.1 Determination of t_0 and assignment of tracks

An essential component in determining the time-of-flight of a particle is the initial time of production, the so-called 't_0'. This could be determined from the information from the LHC machine itself, but the length of the bunches needs also to be taken into account. It is possible to reverse engineer the PID algorithm logic to determine t_0, using all other tracks in the event. By assuming the other tracks in the event are pions and removing the large outliers, the resulting time distribution can be fitted to determine the initial time with a precision of a few picoseconds. This precision should be studied with the full simulation in an environment with multiple primary interactions.

As introduced in Section 4.2, timing information from the TORCH detector could also be used in combination with timing information from other sub-detectors to improve the assignment of tracks to primary interactions. This is of interest more widely than just the tagging algorithms, as correctly identifying the primary interaction is important for any

process resulting in displaced tracks. The study of this will require a reliable simulation of the timing information from TORCH.

5.2   Ghost rejection

Ghost tracks are a consequence of incorrect combination of track stubs from different tracking stations. As the occupancy of the detector increases, the combinatorics of these stubs can result in a fast increase in the number of ghosts. Additional timing information assigned in various sub-detectors may help in identifying the correct combinations and therefore curtail the rapid increase in ghost tracks. If the track entering TORCH does not correspond to a real charged particle with the correct entry position and path-length then there will be no reliable PID hypothesis. The exact extent to which TORCH may contribute to the elimination of ghost tracks could be studied.

6   Conclusions

This document sets out the state of progress in the development of the TORCH detector, both physically and in simulation, and describes studies that have been performed to identify potential performance improvements to LHCb physics.

A successful series of beam tests at the East Hall T9 facility at CERN has been performed, testing two prototype TORCH modules in a beam of protons and pions. The data analysis determines the single photon resolution to be in the range 84–111 ps, which can be compared to the desired time resolution of 70 ps. The incorporation of the TORCH detector into the full LHCb simulation framework is well underway, with preliminary PID performance plots indicating TORCH is able to distinguish pions and kaons with momentum in the range 2–10 GeV/c and protons from lighter particles up to 20 GeV/c.

Initial studies using a stand-alone TORCH simulation have identified a number of key physics areas that would benefit from the improved low-momentum PID performance provided by TORCH. Specific decay modes have indicated improvements in signal efficiency with signal yields increasing by factors of 10% to up to 130%, depending on the extent that PID and momentum requirements are required to control background levels. Additionally, modes have shown improved mis-identification background rejection and reduced efficiency dependence in phase space. The performance of simple, cuts-based tagging algorithms have shown improvements of between 20–30% as a result of the improved low momentum PID efficiency, potentially affecting a large number of analyses. A range of further topics have been identified that will be studied in the future.

References

[1] LHCb collaboration, M. J. Charles and R. Forty, *TORCH: Time of Flight Identification with Cherenkov Radiation*, Nucl. Instrum. Meth. **A639** (2011) 173, arXiv:1009.3793.

[2] LHCb collaboration, A. A. Alves Jr. *et al.*, *The LHCb detector at the LHC*, JINST **3** (2008) S08005.

[3] LHCb collaboration, R. Aaij *et al.*, *Physics case for an LHCb Upgrade II - Opportunities in flavour physics, and beyond, in the HL-LHC era*, arXiv:1808.08865.

[4] LHCb collaboration, R. Aaij *et al.*, *Expression of Interest for a Phase-II LHCb Upgrade: Opportunities in flavour physics, and beyond, in the HL-LHC era*, Tech. Rep. CERN-LHCC-2017-003, CERN, Geneva, Feb, 2017.

[5] BaBar DIRC collaboration, I. Adam *et al.*, *The DIRC particle identification system for the BaBar experiment*, Nucl. Instrum. Meth. **A538** (2005) 281.

[6] Belle-II collaboration, T. Abe *et al.*, *Belle II Technical Design Report*, arXiv:1011.0352.

[7] U. Tamponi, *The TOP counter of Belle II: status and first results*, in *10th Workshop on Ring Imaging Cherenkov Detectors (RICH2018) Moscow, Russia, July 29-August 4, 2018*, 2018, arXiv:1811.04532.

[8] N. Brook *et al.*, *Testbeam studies of a TORCH prototype detector*, Nucl. Instrum. Meth. **A908** (2018) 256, arXiv:1805.04849.

[9] R. Gao *et al.*, *Development of TORCH readout electronics for customised MCPs*, JINST **11** (2016) C04012.

[10] M. Clemencic *et al.*, *The LHCb simulation application, Gauss: Design, evolution and experience*, J. Phys. Conf. Ser. **331** (2011) 032023.

[11] I. Belyaev *et al.*, *Handling of the generation of primary events in Gauss, the LHCb simulation framework*, J. Phys. Conf. Ser. **331** (2011) 032047.

[12] Geant4 collaboration, S. Agostinelli *et al.*, *Geant4: A simulation toolkit*, Nucl. Instrum. Meth. **A506** (2003) 250.

[13] Geant4 collaboration, J. Allison *et al.*, *Geant4 developments and applications*, IEEE Trans. Nucl. Sci. **53** (2006) 270.

[14] I. Belyaev, *Integration of GEANT4 with the GAUDI framework*, , LHCb-TALK-2001-023.

[15] LHCb collaboration, R. Aaij *et al.*, *Measurement of CP asymmetries in two-body $B^0_{(s)}$-meson decays to charged pions and kaons*, Phys. Rev. **D98** (2018) 032004, arXiv:1805.06759.

[16] LHCb collaboration, R. Aaij *et al.*, *Opposite-side flavour tagging of B mesons at the LHCb experiment*, Eur. Phys. J. **C72** (2012) 2022, `arXiv:1202.4979`.

[17] LHCb collaboration, R. Aaij *et al.*, *Precision measurement of the B_s^0–$\overline{B}_s^0$ oscillation frequency in the decay $B_s^0 \rightarrow D_s^- \pi^+$*, New J. Phys. **15** (2013) 053021, `arXiv:1304.4741`.

[18] LHCb collaboration, R. Aaij *et al.*, *New algorithms for identifying the flavour of B^0 mesons using pions and protons*, Eur. Phys. J. **C77** (2017) 238, `arXiv:1610.06019`.

[19] LHCb collaboration, R. Aaij *et al.*, *Observation of $J/\psi p$ resonances consistent with pentaquark states in $\Lambda_b^0 \rightarrow J/\psi p K^-$ decays*, Phys. Rev. Lett. **115** (2015) 072001, `arXiv:1507.03414`.

[20] Y. Gao *et al.*, *Observation of pentaquark-charmonium states seen in $\Lambda_b^0 \rightarrow J/\psi p K^-$ decays*, LHCb-ANA-2015-025.

[21] LHCb collaboration, R. Aaij *et al.*, *Measurement of matter-antimatter differences in beauty baryon decays*, Nature Physics **13** (2017) 391, `arXiv:1609.05216`.

[22] LHCb collaboration, R. Aaij *et al.*, *Determination of the quark coupling strength $|V_{ub}|$ using baryonic decays*, Nature Physics **11** (2015) 743, `arXiv:1504.01568`.

[23] W. Detmold, C. Lehner, and S. Meinel, *$\Lambda_b \rightarrow p \ell^- \overline{\nu}_\ell$ and $\Lambda_b \rightarrow \Lambda_c \ell^- \overline{\nu}_\ell$ form factors from lattice qcd with relativistic heavy quarks*, Phys. Rev. D **92** (2015) 034503.